

ORBITER WINDWARD SURFACE ENTRY HEATING:
POST-ORBITAL FLIGHT TEST PROGRAM UPDATE

M. H. Harthun, C. B. Blumer, and B. A. Miller
Space Transportation and Systems Group
Rockwell International
Downey, California

SUMMARY

Correlations of orbiter windward surface entry heating data from the first five flights are presented with emphasis on boundary layer transition and the effects of catalytic recombination. Results show that a single-roughness boundary layer transition correlation developed for spherical-element trips works well for the orbiter tile system. Also, an engineering approach for predicting heating in nonequilibrium flow conditions shows good agreement with the flight test data in the time period of significant heating. The results of these correlations, when used to predict orbiter heating for a high-cross-range mission, indicate that the thermal protection system on the windward surface will perform successfully in such a mission.

INTRODUCTION

The design of the orbiter thermal protection system (TPS) was based on the following logic: the most severe operational mission was selected to define the design heating environments, but nominal trajectory parameters, nominal heating methods, nominal material properties, and an aerodynamically smooth surface were assumed in order to save weight. Safety margins for the flight test program were created by the lower orbit inclinations and reduced cross range requirements during these flights, which reduced the severity of the thermal environments. The aerothermodynamic objective of the flight test program was to obtain data to update the heating methodology, which then could be used to support verification of the TPS for operational use. To this end, development flight instrumentation (DFI) was installed on the vehicle to obtain data in critical locations. Data from the flight test program were expected to demonstrate that margins would also exist for the operational missions, even though a nominal design approach had been taken.

This paper presents the projected operational capability of the TPS (specifically the windward surfaces) in light of the lessons learned from the flight test program regarding entry aerodynamic heating.

PRECEDING PAGE BLANK NOT FILMED

SYMBOLS

C	constant in equation 7
C_{P_f}	frozen specific heat
g	gravitational constant
h	local heat transfer coefficient
H	enthalpy
k	roughness element height
L	orbiter reference length
M	Mach number
N	constant in equation 7
P	local pressure
q	heat flux
Re_k	trip Reynolds number, $\rho_\delta u_\delta k / \mu_\delta$
Re_{x_k}	trip position Reynolds number, $\rho_\delta u_\delta x_k / \mu_\delta$
Re_{δ^*}	displacement thickness Reynolds number at the trip position for effective tripping, $\rho_\delta u_\delta \delta^* / \mu_\delta$
Re_θ	momentum thickness Reynolds number, $\rho_\delta u_\delta \theta / \mu_\delta$
R_0	universal gas constant
T	temperature
u	velocity
x	axial coordinate
x_k	trip position measured from stagnation point
x_t	transition position measured from stagnation point
y	spanwise coordinate
Z	compressibility
α	angle of attack
δ^*	displacement thickness of boundary layer
θ	momentum thickness of boundary layer

ρ density
 μ viscosity
 η defined in equation 6
 γ_R defined in equation 7

Subscripts

aw adiabatic wall
 D dissociation
 eff effective
 eq equilibrium
 f frozen
 ne nonequilibrium
 w wall conditions
 δ boundary layer edge conditions

FLIGHT TEST PROGRAM

Flight Conditions

The Orbital Flight Test (OFT) program consisted of four flights, STS-1 through -4. Aerodynamic heating data were acquired by a DFI system with an on-board recorder. The fifth flight, STS-5, although an operational flight, also provided aeroheating data since the DFI system was utilized. In all five flights, the orbiter entered the atmosphere from low Earth orbits at inclinations ranging from 28.5 deg to 40 deg. Peak heating generally occurred when the vehicle angle of attack was 40 deg, and the thermal equivalent cross range flown was approximately 720 nmi.

Instrumentation

The entry aerodynamic heating data on the lower surface of the orbiter were obtained primarily from thermocouples installed in the outer surface of the high-temperature reusable surface insulation (HRSI) and in contact with the reaction cured glass (RCG) tile coating. These instruments, fabricated from a 10-mil platinum-platinum 13-percent rhodium wire, were located as shown in figure 1. In addition to the thermocouples, the lower fuselage surface was instrumented with pressure taps and calorimeters. A more detailed description of the DFI system can be found in reference 1.

RESULTS AND DISCUSSION

Data from the flight test program show that heating on the upper surfaces was generally less than predictions based on wind tunnel test data. The exception is the area influenced by the vortex emanating from the wing-glove/body junction. This area includes the fuselage side, payload bay door, and orbital maneuvering subsystem (OMS) pod. Possible reasons for the higher heating in flight are presented in reference 2.

The lower surfaces experienced less heating than expected during flight due to two phenomena: delayed boundary layer transition and reduced catalytic recombination. Therefore, this paper focuses on the knowledge gained from the flight test program with regard to these two topics.

Boundary Layer Transition

One of the major considerations in defining the entry heating environment was the time at which boundary layer transition occurs. The design philosophy was to specify the heating environment with a "smooth surface" transition. Smooth surface transition was defined as the transition conditions measured on a smooth wind tunnel model and correlated and extrapolated to flight by using $Re_{\tau}/M_{\infty} = f(\text{angle of attack, body location})$. It was anticipated that the wind tunnel would provide a conservative transition value due to free-stream turbulence and that transition during flight would be induced by surface roughness.

Orbiter Surface Description. The TPS on the lower surface of the orbiter is composed primarily of insulating tiles with nominal surface dimensions of 6 in. by 6 in. The tiles are spaced by nominal gaps of 0.045 in. during installation to provide clearance for differential thermal expansion (contraction) between the tile and the orbiter's aluminum structure during flight. The tile edges are rounded to avoid stress concentrations in the glassy coating. Some tile surface irregularities exist due to manufacturing techniques or to surface slumping when the tile coating is fired; in addition, installation tolerances result in steps between tiles. The foregoing is not the description of an aerodynamically smooth surface; in fact, the many combinations of steps, gaps, and tile irregularities produce an incredibly complex surface in terms of roughness definition.

Several types of measurements were used to inspect the orbiter surface. Steps and gaps between adjacent tiles were measured after installation. Subsequent visual inspections indicated that in a significant number of cases, the step measurements did not identify the worst steps. As a result, a "profilometer" was built to measure the tile surface. The profilometer follows the principle of microsurface analyzers but on a much larger scale. It traces a path 50 in. long on the orbiter surface with three transducers spaced 0.25 in. laterally. An electronic plotter simultaneously plots the results, expanding the vertical scale 25 times so that a 0.001-in. surface displacement may be resolved.

A typical trace is shown in figure 2. Profile locations were selected on the basis of a visual inspection of the surface, always looking for the worst TPS installations. A set of 16 of these locations was also measured after each of the first four flights. No significant changes occurred from flight to flight at these locations. Measurement variations within 0.015 in. were observed, which is almost within the variation of repeated setups at the same location.

During the evolution of the thermal protection system, exploratory wind tunnel tests were performed on smooth orbiter models that were grooved to simulate tile gaps. It was discovered that grooves parallel to the surface streamlines produced strong boundary layer tripping disturbances whereas grooves perpendicular to streamlines produced much weaker disturbances. Subsequent experiments indicated that a 15-deg angle between gap and flow direction was sufficient to avoid the parallel-gap tripping effect. These observations resulted in the tile orientation pattern shown in figure 1.

Analysis. To develop analytical tools to define allowable TPS installation tolerances and further relate the completed orbiter surface configuration to the observed transition during flight, existing wind-tunnel-based boundary layer transition research was used. As previously stated, it was presumed that transition would be caused by single or isolated roughness elements that are three dimensional in character. The reasoning that leads to this assumption is as follows.

First, it has been demonstrated (ref. 3) that in supersonic flow three-dimensional roughnesses (spheres) are more effective trips than two-dimensional roughnesses (wires perpendicular to flow). By analogy, tile edges where the step and gap are uniform may be thought of as two-dimensional roughnesses and tile corners or intersections as three-dimensional roughnesses. If the tile edge and corner steps are the same, then the corner should produce the dominant disturbance. Also, wind tunnel tests (ref. 4) showed that spacing three-dimensional roughnesses laterally at a distance of four roughness heights ($4k$) was sufficient to prevent interaction between roughnesses; that is, it allows each element to act as if it were the only roughness element present. The maximum anticipated roughness is on the order of $k = 0.1$ in.; therefore, disturbance spacing greater than 0.4 in. should not cause interaction.

Finally, figure 3 shows schematically how three-dimensional roughness size variation affects transition location. In section A of figure 3, between (1) and (2) the roughness has very little effect on the natural or smooth wall transition, indicating that the roughness disturbances do not dominate the boundary layer before they decay. The region between (2) and (3) is characterized by a small change in roughness size, causing a large change in transition position. The curve to the right of (3) again shows only a small change in transition position with roughness size when transition is close to the trip. Point (3) is defined as the "effective trip" size, i.e., the smallest trip that will cause transition near the trip. In this discussion, only the left side of figure 3, section A, up to point (3) is of concern. Section B of figure 3 shows the effect of increasing trip size. The boundary layer is very discriminating as to the roughness sizes that affect transition. Since the roughness distribution was not expected to be uniform, a relatively small number of discrete roughnesses were expected to cause transition, and there was a low probability that these disturbances would interact with one

another. The conclusion was that single-roughness-element transition research would be an appropriate basis for the analytical tools. (It will be shown later that the observed transition patterns on the orbiter are consistent with the above assumptions.)

Equation 6 of reference 5 is

$$Re_k = 33.4 \left[1 + 0.90 \left(\frac{T_w}{T_\delta} - 1 \right) + 0.28 \left(\frac{T_{aw}}{T_\delta} - 1 \right) \right] Re_{x_k}^{1/4} \quad (1)$$

which represents the conditions for an effective spherical element trip. This equation is for flow on a cone and includes variations in Mach number and heat transfer. Reference 5 also notes that the bracketed term in equation 1 is nearly equal to $(\delta^*/x_k) / Re_{x_k}$. Empirically, equation 2 represents a slight improvement:

$$\frac{\delta^*}{x \sqrt{Re_{x_k}}} = 1.09 \left[1 + 0.90 \left(\frac{T_w}{T_\delta} - 1 \right) + 0.28 \left(\frac{T_{aw}}{T_\delta} - 1 \right) \right] \quad (2)$$

Substituting equation (2) into equation (1) yields

$$k/\delta^* = 30.7 Re_{x_k}^{-1/4} \quad (3)$$

which also includes heat transfer and compressibility effects for flow over a cone. Equation 3, which matches the data of references 4 and 5 about as well as the previous equations, will be used to extrapolate to orbiter flight conditions because of its simplicity. Fortunately, the assumption of corical flow also is a good approximation for the orbiter lower surface for $x/L \leq 0.5$.

Figure 4 is a typical curve of effective roughness size versus streamwise location along the orbiter centerline at a specific flight condition as predicted from equation 3. The displacement thickness (δ^*) was calculated by using a finite-difference boundary layer computer code called GLTS (ref. 6). Obviously, the nose and wing leading edge are the most critical regions for surface roughness.

Wind Tunnel Tests. Wind tunnel tests were performed at Arnold Engineering Development Center Tunnel B at $M_\infty = 8$ to verify the applicability of equations 1 or 3 for the orbiter configuration. Those tests used a 0.04-scale model of the orbiter forebody ($x/L \leq 0.5$). For the first series of tests, spherical roughnesses were mounted on the model at $x/L = 0.05, 0.11, \text{ or } 0.17$. The models were solid copper forward of the trip to provide an isothermal boundary layer from the stagnation point to the roughness. Aft of the trip, the models were made of an alumina-filled epoxy, and the phase-change paint technique was used to obtain transition data. The roughness elements were spheres with diameters of 0.015, 0.020, 0.025, and 0.031 in. These data are compared with the cone data of reference 5 in figure 5. The second series of tests replaced the spherical roughness elements with a simulated tile array, including gaps between the tiles, as shown in figure 6. One tile in the array was displaced by shimming to create a step. Steps varied from 0 to 0.025 in. at 0.005-in. increments in the previously mentioned x/L stations. Gaps surrounding the stepped tile were 0, 0.010, or 0.020 in.

The results of this series of tests were less definitive than the results for the spherical roughness tests; however, several conclusions were made: (1) increasing the gap surrounding the stepped tile increased the tripping effect of the step; (2) with a 0.010-in. gap around the stepped tile, a step equal to approximately one half of the spherical roughness diameter (height) produced an equivalent transition pattern; and (3) the effect of the gap was most pronounced at the forward test station (i.e., $x/L = 0.05$). One variable that was not included was the tile edge radius. The model tile edges are essentially sharp (as machined), whereas the orbiter tile edge radius varies from about 0.050 to 0.100 in., or about the same as the observed steps. The edge radius may also be a significant variable when the step, edge radius, and the adjacent gap are all roughly the same dimension. Reference 7 suggests that increasing the solid volume at the top of the trip (i.e., reducing the edge radius) increases the effectiveness of the trip; however, the observed factor of two in trip size is much larger than trip-shape-factor effects previously observed.

Flight Test Results. The orbiter flight test program provided a boundary layer transition experiment of unprecedented proportion. Five flights were made with the DFI system operating. Transition-sensing instrumentation on the lower surface consisted of 94 platinum-platinum, 13-percent rhodium thermocouples installed in the tile outer surface coating and distributed over the left side of the orbiter with one thermocouple on the right wing tip as shown in figure 1. Data were recorded for each instrument at one-second intervals throughout the entry. A typical surface-temperature-versus-time record is shown in figure 7. The surface temperature is practically equal to radiation equilibrium temperature. The DFI data were recorded on board and telemetered in real time. Telemetered data were restricted to the latter part of entry because the orbiter was out of range of the receiving antennas early in the entry. On flights STS-1 and -4, failure of the on-board recorder limited the data.

In figure 7, the beginning of transition is the departure from the laminar temperature at 1,263 sec; the end of transition is the attainment of the turbulent temperature at 1,280 sec. The beginning of transition is used hereafter to correlate transition events. The transition interval is the difference between the beginning and end of transition and is characteristically less than 30 sec for flight test data, which represents a change in the Reynolds number of less than 20 percent. This abrupt transition zone is one indication of roughness-induced transition. Another indication of roughness-caused transition is the sudden forward movement illustrated in section A of figure 3. For the flight test data, roughness-caused transition is manifested as the simultaneous transition over some region of the surface observed in the data. Section B of figure 3 shows that transition caused by an effective roughness originates from a point somewhat downstream of the roughness and then spreads as a wedge of turbulence. This wedge crosses streamlines at a constant angle between 5 deg and 7 deg for supersonic boundary layer edge Mach numbers from 2 to 4, respectively (ref. 3). For a conical flow, the turbulent spreading still crosses streamlines at the above angle, but the turbulent front takes on a curved shape due to the streamline spreading. To map the transition regions on the orbiter, regions of constant transition time were associated with one tripping event. Again, the results were consistent with the assumption that single roughness elements cause transition.

Figures 8 through 12 show patterns developed from the flight test data. A spreading angle of 7 deg (assuming a conical flow field) appears to best fit the data although some variations might be expected due to surface Mach number and surface flow field variations with orbiter angle of attack at the transition time. The spacing of instruments also causes some uncertainty in the position of the transition fronts. Thermocouple locations are indicated on the maps. Surface streamline patterns were developed from contamination streaks on the TPS surface after STS-1. These patterns agreed with wind tunnel oil flow patterns used for the conical flow field assumption for $x/L \leq 0.5$. Streak patterns were used for $x/L > 0.5$.

For the first flight, STS-1, surface temperature data were only available after 1,050 sec entry time (entry time = 0 sec at altitude = 400,000 ft) due to a failure of the on-board recorder. At the time of data acquisition, the flow on the aft fuselage and right wing tip instruments was turbulent. Postflight inspection revealed a gouge in a tile on the right nose landing gear door (NLGD) that was approximately 8 in. long x 1 in. wide x 1 in. deep. Plotting the turbulent spreading from this anomaly gives the pattern shown in figure 8. Transition time for this roughness was set at about 1,000 sec based on an increase in the axial force coefficient along with an elevon asymmetry indicating higher drag on the right side. The asymmetry disappeared at 1,252 sec when the left-hand nose tripped. The tripping event at 1,252 sec is significant because it was repeated for flights STS-1, -2, -3, and -5, and because it was the event that affected the largest surface area on subsequent flights. It is observed that transition is propagated along the wing stagnation streamline (i.e., transition along the wing leading edge occurs at the same time as transition on the forward fuselage). After the flight, the left NLGD surface was inspected visually for large tile steps. The largest apparent step, measured at 0.085 in., was at a lateral tile corner at $x/L = 0.056$ and $y = 10$ in. This is the projection shown in the profilometer trace in figure 2. Surprisingly good agreement exists between this roughness location and the forward extrapolation of the turbulence spreading zone. Equation 3 gives an effective roughness height of 0.080 in. for this location at 1,252 sec. It appears that equation 3 works quite well without an adjustment for roughness shape factor. Two other forward fuselage tripping events occurred at 1,140 sec and 1,230 sec (fig. 8).

Figure 8 also shows that transition occurs on the wing at times ranging from 1,150 sec to 1,235 sec. The number and location of thermocouples in each turbulent wedge do not define the apex of the wedges accurately enough to identify a specific roughness for each tripping event; however, the tripping appears to be related to the wing leading edge or the tile interface region immediately behind the leading edge. The boundary layer on the swept-wing leading edge is already unstable, indicating that the allowable roughness on the leading edge must be less than in the nose region to produce the same transition time, assuming similar roughnesses exist on the wing and on the fuselage. The inboard turbulent wedge is caused by the main landing gear door outboard edge. Note the two transition times (i.e., 1,193/1,226 sec). This notation designates a significant transition event followed by a return to or movement toward a laminar surface temperature, followed by a second transition. The last time is the beginning of the transition that stays turbulent. In this instance, a dip in the angle of attack causes the roughness not to be an effective trip from 1,200 sec to 1,226 sec. Transition on the elevons occurs from before data acquisition at 1,050 sec to 1,155 sec and can be associated with the wing/elevon gap and elevon deflection angle.

The STS-2 and STS-1 trajectories were similar, and as figure 9 shows, the transition patterns and times were also similar. The primary difference was the absence of the gouge on the right hand nose during flight two. Significantly early transition occurs only downstream of the external tank attachment door and on the body flap of the aft fuselage for STS-2. The left NLGD tripping event occurs at 1,263 sec in STS-2 and appears to extrapolate forward to the same roughness location as in STS-1. An aft fuselage transition at 1,250 sec is extrapolated forward to the right NLGD; however, uncertainty in this location is noted. The wing pattern is substantially the same as in STS-1. The early transition on the body flap (i.e., between 500 sec and 700 sec) can be attributed to boundary layer separation caused by the flap's 15 deg down deflection.

STS-3 results (fig. 10) are similar to STS-1 and STS-2 with earlier transition times due to trajectory differences. Also, the transition pattern is somewhat more complicated. A substantial portion of the fuselage and wing transition occurred at 1,180 sec but appeared tentative and finally occurred 13 sec later. The origin of this event is assigned to the NLGD centerline thermal barrier. The left NLGD tripping occurred cleanly at 1,293 sec and overran the tentative 1,180 sec event. Right side events occurred at 1,112/1,145 sec and at 1,162 sec with the double time explainable as an α transient. The wing pattern closely resembles flights one and two. Right-hand-side transition events must be inferred from downstream patterns that cross the centerline or affect the right-hand wing tip.

Results from STS-4 (fig. 11) are notably different from the previous flights in that transition occurred over almost the entire lower surface due to a single tripping event at 1,030 sec. The apex of the transition appears to be in line with the microphone on the left NLGD. One significant difference was that transition occurred when the angle of attack was 40 deg rather than 32 to 34 deg for STS-1 through -3.

The STS-5 transition map is shown in figure 12. A right-side event is noted at 1,093/1,121 sec on the aft fuselage whereas the right wing tip tripped only at 1,121 sec, indicating that the 1,093 sec event is not far enough forward to spread onto the wing. The 1,125-sec event is consistent in location with the left-hand NLGD tripping on flights 1 through 3. Tripping occurred near the front of the left-hand NLGD at 1,145 sec. Less wing tripping was evident during STS-5 than on the first three flights.

To compare data from each instrumented flight, equation 3 was used to calculate the size of a fictitious roughness at $X/L = 0.1$ at the time of tripping in the left NLGD region. Results are presented in table I. The calculations indicate a nearly constant effective roughness size ($k_{AV} = 0.113$ in.) for flights -1 through -3 and -5, even though the trajectory parameters changed substantially. The larger roughness ($k_{eff} = 0.133$ in.) calculated for STS-4 has not been explained, but this roughness size is large enough to cause transition before the observed wing tripping times on the other flights. This could explain the single-event tripping in STS-4.

It is concluded that: (1) a single roughness site on the left NLGD tripped the boundary layer on four of the five flights; (2) this roughness (k_{eff}) remained essentially unchanged through the flight test program; (3) transition from this roughness was obscured by earlier transition from a larger roughness in STS-4; and (4) an analytical method that predicts the effective roughness size has been extended from wind tunnel conditions to entry flight conditions.

Catalytic Recombination

The design of the orbiter TPS was accomplished by predicting heating based on the assumption of equilibrium flow. The methods used are described in reference 8. The approach to predict heating on the lower surface of the orbiter consisted of breaking the vehicle down into simple geometric shapes, predicting the heating for the assumed shape and modifying the prediction to match wind tunnel data. The resulting correlation was extrapolated to flight conditions using real-gas properties. The methods are incorporated in the Rockwell International Aeroheating Computer Program (ref. 9) which was formulated as a design instrument to estimate ascent or entry heating for simple geometric shapes. An inability to predict non-equilibrium boundary layer heating and a lack of knowledge about the catalytic behavior of the TPS tile coating precluded a design approach based on these phenomena. However, results from plasma arc heater tests during the TPS development test program indicated the inhibiting characteristics of the tile baseline coating may reduce aerodynamic heating. During the test program, the heating to the TPS coating in a plasma environment could be approximated by using

$$\dot{q}_{\text{TEST}} = \dot{q}_{\text{eq}} \left[\frac{H_{\text{aw}} - H_{\text{w}} - \eta H_{\text{D}}}{H_{\text{aw}} - H_{\text{w}}} \right] \quad (4)$$

where η was found to be 0.7 ± 0.1 (ref. 10). However, characterization of the dissociated nonequilibrium gases produced by the arc heaters was difficult and the tile coating was often contaminated. These phenomena precluded a confident update of the aeroheating prediction methods prior to the OFT program.

Analysis. Flight test data from STS-1 were acquired only during the last part of the entry trajectory. As a result, little was learned relative to the catalytic recombination characteristics of the orbiter TPS. During the second flight, data were acquired throughout the entry profile. The results showed that during the laminar flow regime, the heating over the fuselage lower surface was significantly less than predicted by the equilibrium heating methods (fig. 13). This data presented good insight into the potential reduction of aeroheating due to the inhibiting characteristics of the TPS coating. In addition, in STS-2, the orbiter experiments (OEX) catalytic surface effects (CSE) experiment sponsored by the NASA Ames Research Center was initiated. The results from this experiment dramatically illustrated the significance of catalytic recombination on the orbiter entry heating. These experiments were continued in subsequent flights and the results reported in other sources such as references 11 and 12.

To estimate the effects of a partially catalytic wall on aeroheating, equation 4 was applied to orbiter entry with consideration for frozen boundary layer properties:

$$\dot{q}_{\text{ne}} = \dot{q}_{\text{eq}} \left[\frac{H_{\text{aw}} - C_{\text{p}_f} T_{\text{w}} - \eta H_{\text{D}}}{(H_{\text{aw}} - H_{\text{w}})_{\text{eq}}} \right] \quad (5)$$

By reviewing and interpreting the results of research in the field of nonequilibrium aeroheating, a relationship was obtained for η in terms of flight variables and the thermochemical properties of the TPS tile surface:

$$\eta = 1 - \frac{\rho_g Y_R}{\rho_{e1} \sqrt{2\pi R_0 Z_f T_w}} \quad (6)$$

The variable, Y_R , represents the number of recombined atoms of oxygen and nitrogen normalized by the total number of uncombined atoms at the edge of the boundary layer. An Arrhenius relation was assumed for Y_R :

$$Y_R = N \text{ EXP } (-C/T_w) \quad (7)$$

The DPI data from STS-2 was used to determine the values for N and C . The resulting correlation is

$$Y_R = 0.05787 \text{ EXP } (-6876/T_w) \quad (8)$$

The nonequilibrium aeroheating was estimated by using equations 5, 6, and 8.

Flight Test Results. When this semi-empirical technique is applied to the STS-2, trajectory results are as shown in figures 13, 14, and 15, where surface temperature data and predictions are compared as a function of time at three stations along the fuselage lower centerline. Figure 13 also includes a prediction for equilibrium flow using the methodology referred to earlier. Figure 16 shows a crossplot of figures 13, 14, and 15 at two times during the trajectory. The second time cut selected was 1,200 sec since this is just prior to the time of boundary layer transition and the prediction technique for nonequilibrium heating has been assumed to be valid only during the laminar flow regime. The maximum deviation between the prediction model and data for these two time cuts is approximately 7 percent.

The results for STS-3 are shown in figures 17, 18, 19, and 20, and in general are similar to the results shown for STS-2.

Both figures 16 and 20 show excellent agreement between estimated surface temperature and measured flight temperature distributions for the later flight times. These times correspond to the onset of flow transition and the approach of the free stream to equilibrium chemistry conditions. This would enhance the validity of the equilibrium heating technique. The results of analyses of STS-5 data are still preliminary; however, a comparison of the overall results with those from previous flights is included in table III.

Table II presents average temperature deviations between estimated and measured values in the time period between 400 and 1,100 sec for three orbiter flights, STS-2, -3, and -5. These data are remarkably consistent and demonstrate the accuracy of the correlation (equation (5)) based on STS-2 flight data.

At the beginning of entry, 0 to 300 sec, the results from this engineering technique displayed larger differences compared to flight data than in the time period from 400 to 1,100 sec. This may be for two reasons: the application of a continuum flow model partially modified to account for low density flow, and the application of a radiation equilibrium assumption during the time of significant conduction into the TPS as compared to the incoming convective heating. However, during this time period, the impact of aeroheating on heat load (structure temperature) or peak surface temperature is not of major significance.

TPS Capability Projection

A preliminary analysis has been conducted to project the capability of the orbiter TPS for flying high-cross-range missions using the results from the OFT program as discussed in this paper and applying them to the computed trajectory for such a mission. The mission selected was entry from an orbital inclination of 104 deg with a cross-range requirement of 940 n.mi. achieved by flying a 38 to 28 deg angle of attack profile. Using the heat load of a one-foot-radius sphere as an indicator, this mission is approximately 50 percent more severe than the worst of the OFT flights and approximately 30 percent more severe than the TPS design trajectory (fig. 21). Nevertheless, based on the favorable results of the OFT program, it is projected that the windward surface TPS has the capability to accomplish this mission. This conclusion is drawn by comparing the predicted maximum surface temperatures and heat loads for this mission with TPS design values. As illustrated in table III, the maximum surface temperatures do not exceed the design values. At most locations, the heat loads (driver for structure bondline temperature) are less than the design values. Although there are locations where the design values are exceeded, the vehicle can accommodate these environments satisfactorily. Additional flight data and analyses are required to verify the TPS capability.

CONCLUDING REMARKS

Consistent and reliable correlations of the orbiter flight test heating data were obtained relative to boundary layer transition and catalytic recombination. The application of these correlations in predicting the heating of the orbiter for a high-cross-range mission indicates that the TPS on the windward surfaces has the capability for successfully performing this mission. This result tends to validate the unique design approach used for the orbiter TPS.

An understanding of boundary layer transition and catalytic recombination is not only significant for verifying the orbiter TPS, but is also helpful in the design of effective thermal protection systems for future entry vehicles. Therefore, it is recommended that high priority be given to the continued analysis and understanding of these phenomena.

REFERENCES

1. Smith, J. A., "STS-3 Structural and Aerodynamic Pressure, Aerothermodynamic and Thermal Protection System Measurement Locations," SMD/NASA/JSC, No. 17889, Jan. 15, 1982.
2. Haney, J. W., "Orbiter Entry Heating Lessons Learned From Development Flight Test Program," Shuttle Performance: Lessons Learned, NASA CP-2283, Part 2, 1983, pp. 719-951.
3. Van Driest, E. R. and W. D. McCauley, "The Effect of Controlled Three-Dimensional Roughness on Boundary Layer Transition at Supersonic Speeds," Journal of the Aerospace Sciences, Vol. 27, No. 4, pp. 261-272, Apr. 1980.

4. Van Driest, E. R. and C. B. Blumer, "Boundary-Layer Transition at Supersonic Speeds - Three-Dimensional Roughness Effects (Spheres)," Journal of the Aerospace Sciences, Vol. 29, No. 8, pp. 909-916, Aug. 1962.
5. Van Driest, E. R. and C. B. Blumer, "Boundary-Layer Transition at Supersonic Speeds: Roughness Effects with Heat Transfer," American Institute of Aeronautics and Astronautics Journal, Vol. 6, No. 4, pp. 603-607, Apr. 1968.
6. Waiter, S. A. and L. P. LeBlanc, "Solution of the Equations of the Compressible Boundary Layer (Laminar, Transition, Turbulent) by an Implicit Finite Difference Technique," Astronautica Acta, Vol. 16, pp. 265-275, 1971.
7. Morrisetti, E. L., D. R. Stone, and A. H. Whitehead, "Boundary Layer Tripping with Emphasis on Hypersonic Flows," Viscous Drag Reduction, Plenum Press, N.Y., pp. 33-51, 1969.
8. Lee, D. E. and M. E. Harthun, "Aerothermodynamic Entry Environment of the Space Shuttle Orbiter," AIAA Paper 82-0821, presented at the AIAA/ASME 3rd Joint Thermophysics Fluids, Plasma and Heat Transfer Conference, St. Louis, MO, June 7-11, 1982.
9. Miller, B. A.; "XF0002 Aeroheating Computer Program Engineering Description and User's Guide," SOD 80-0150, Aug. 1982 Rev.
10. Miller, B. A.; "Coldarc-Dissociated Air Flow Effects During Plasma Arc Testing," Cosmic Program Abstract, Computer Software Management and Information Center, University of Georgia, Nov. 1982.
11. Stewart, D. A., J. V. Rakich, and M. J. Lanfranco, "Catalytic Surface Effects Experiment on the Space Shuttle," AIAA Paper 81-1143, June 1981.
12. Rakich, J. V., D. A. Stewart, and M. J. Lanfranco, "Results of a Flight Experiment on the Catalytic Efficiency of the Space Shuttle Heat Shield," AIAA Paper 81-0944, June 1982.

ORIGINAL PAGE IS
OF POOR QUALITY

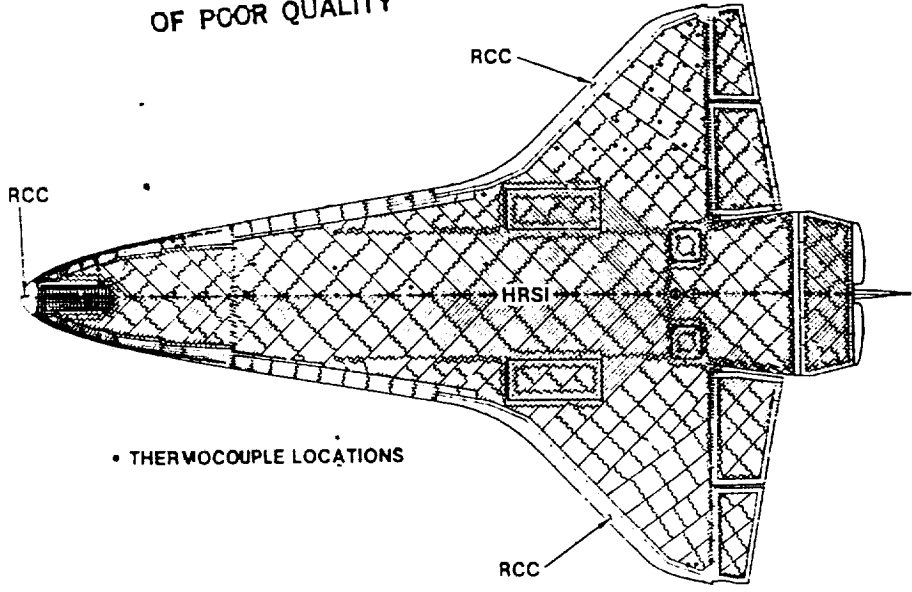


Figure 1.- Orbiter lower surface tile pattern and surface thermocouple layout.

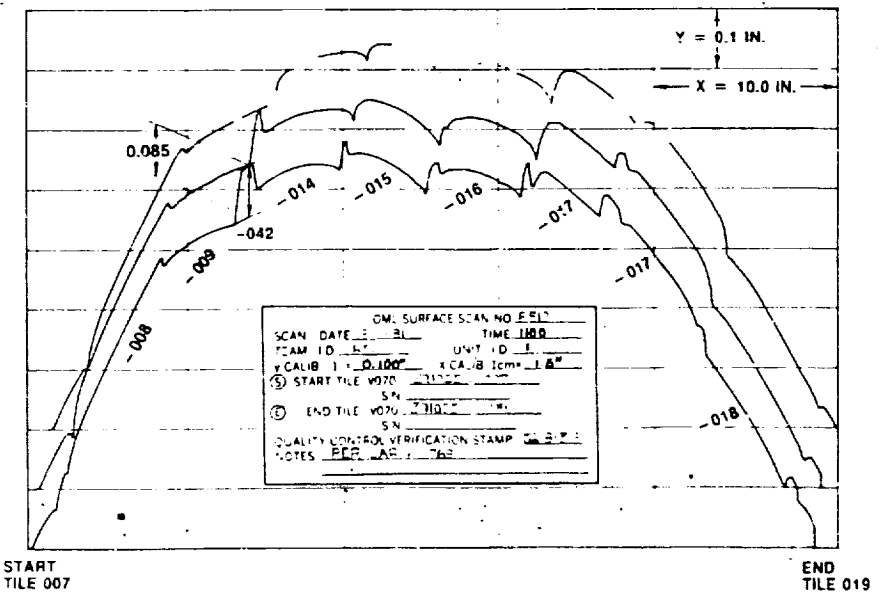


Figure 2.- Profilometer trace on nose landing gear door.

ORIGINAL PAGE IS
OF POOR QUALITY

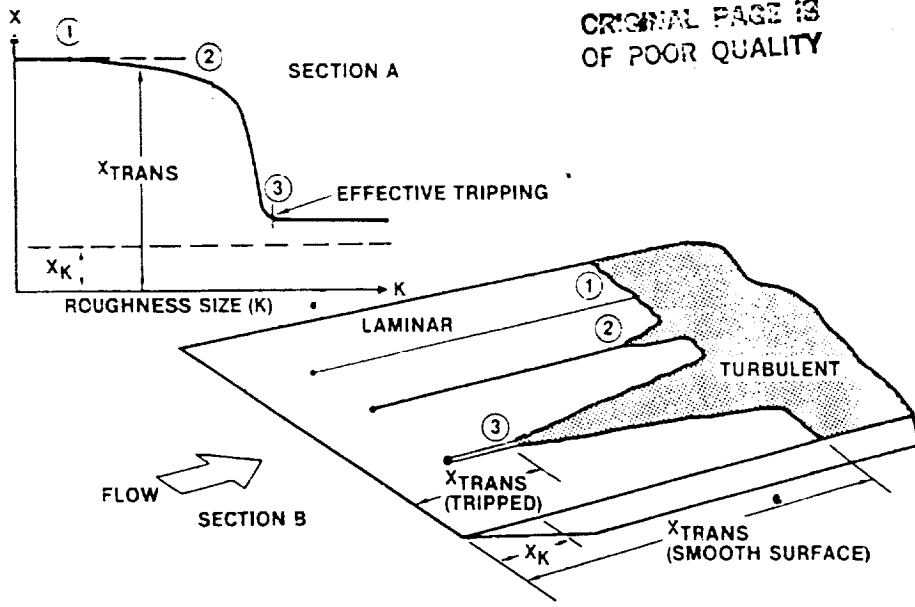


Figure 3.- Description of roughness-produced transition.

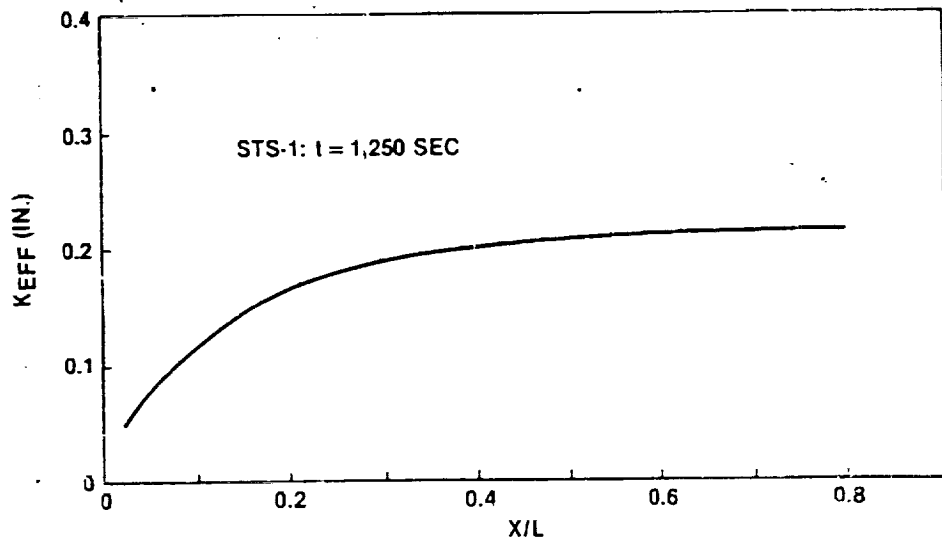


Figure 4.- Typical variation of effective roughness with length.

ORIGINAL PAGE IS
OF POOR QUALITY

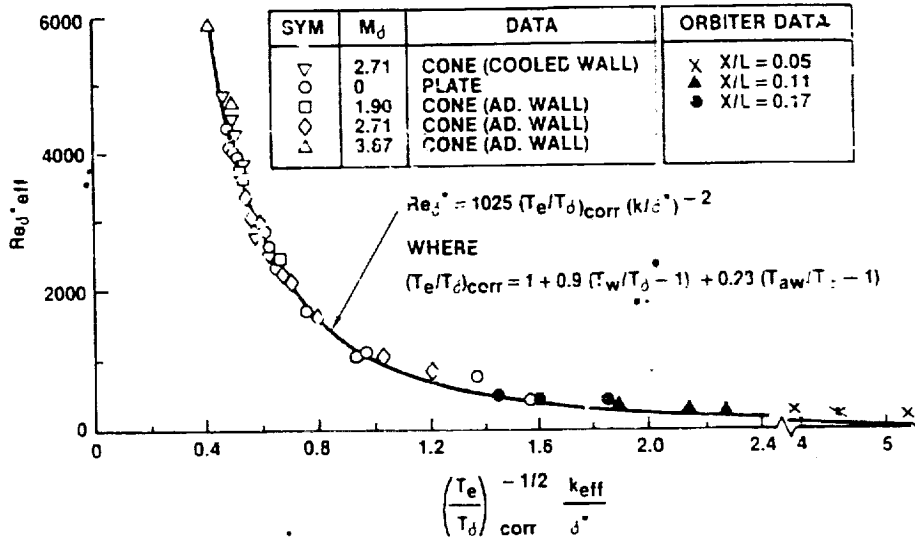


Figure 5.- Composite plot of effective transition data including compressibility and cooling.

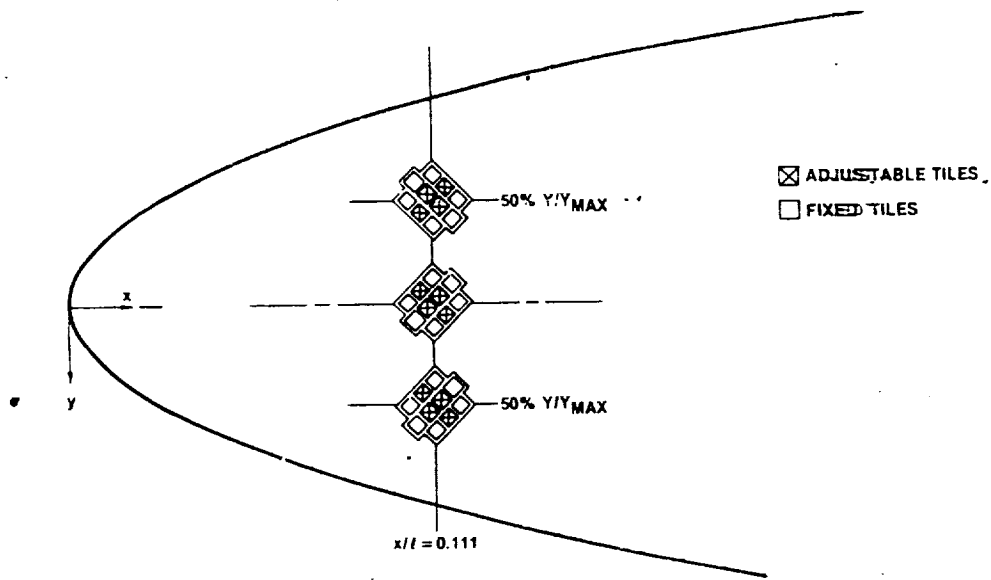
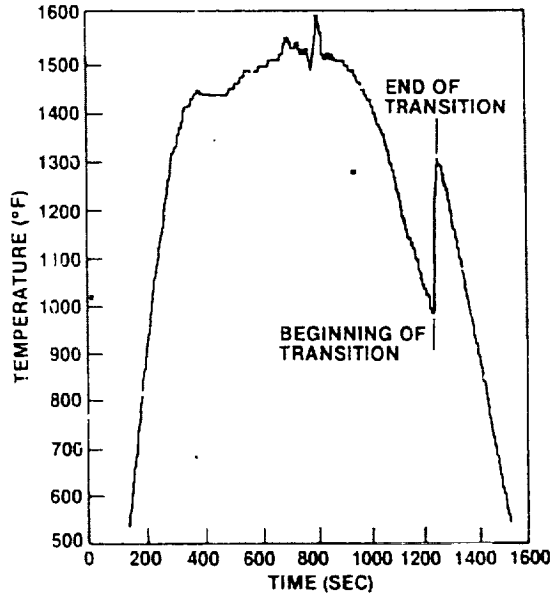


Figure 6.- Tile cluster layout.



ORIGINAL PAGE IS
OF POOR QUALITY

Figure 7.- STS-2 surface temperature history ($X/L = 0.30$; $Y/L = 0.30$).

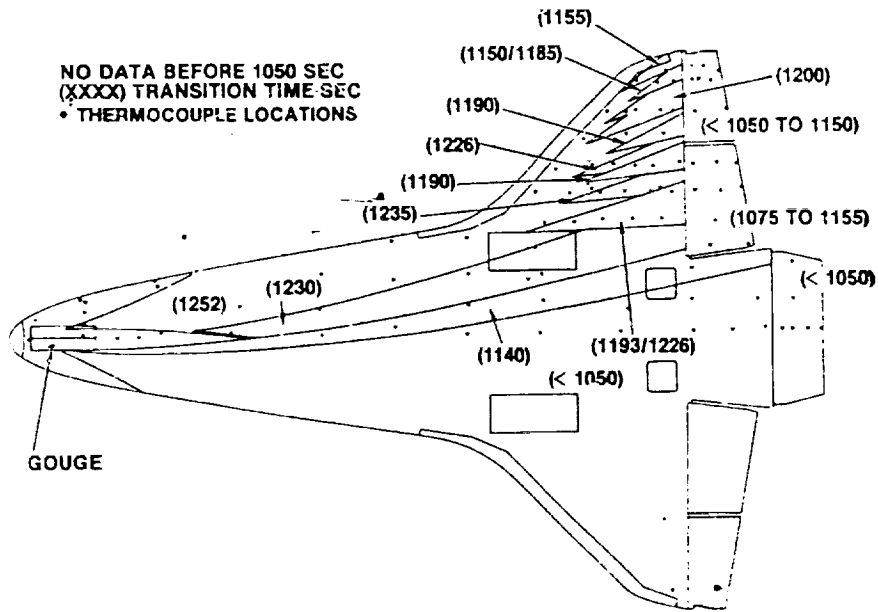


Figure 8.- STS-1 transition map.

ORIGINAL PAGE 13
OF POOR QUALITY

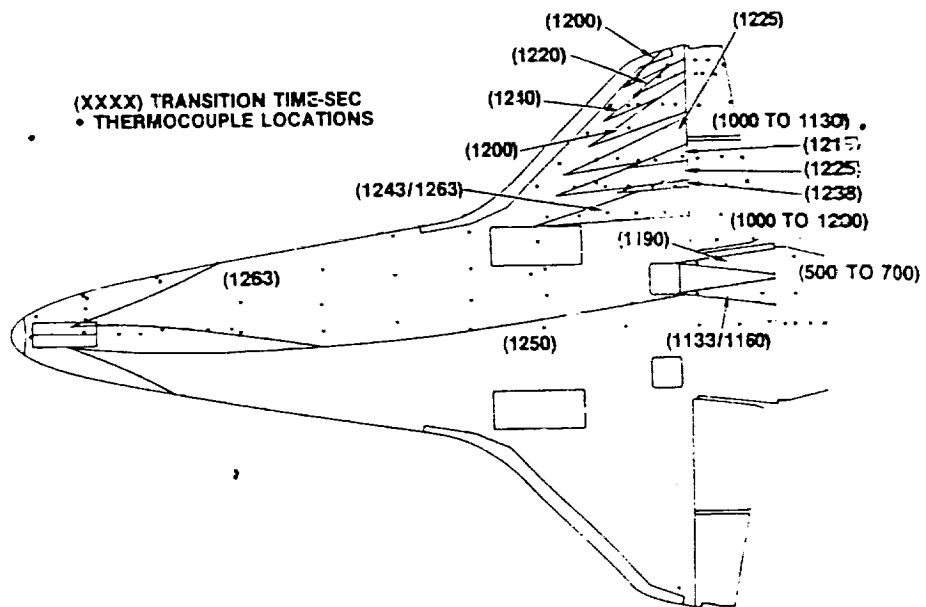


Figure 9.- STS-2 transition map.

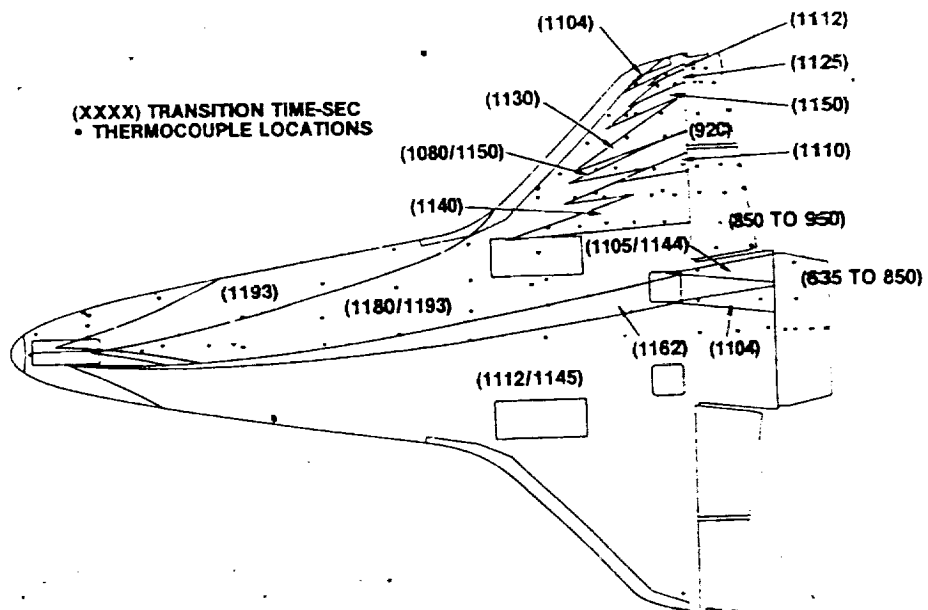


Figure 10.- STS-3 transition map.

ORIGINAL PAGE 13
OF POOR QUALITY

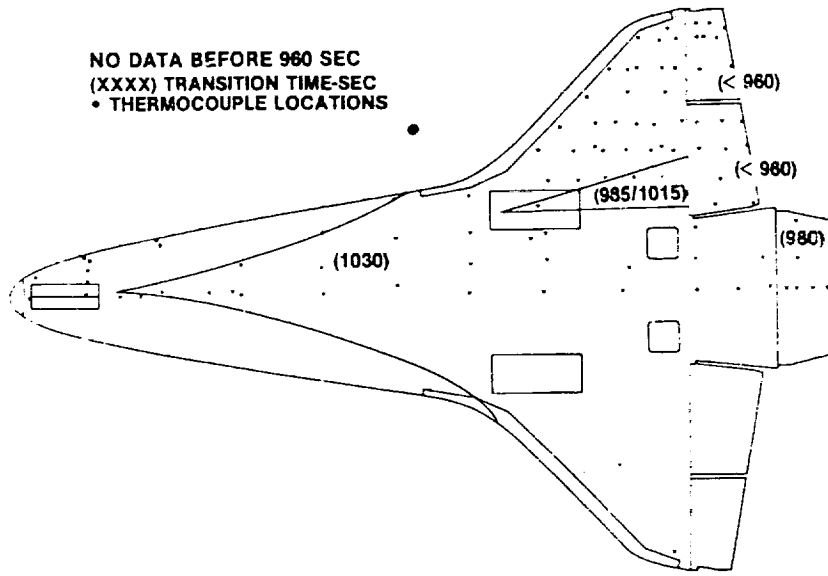


Figure 11.- STS-4 transition map.

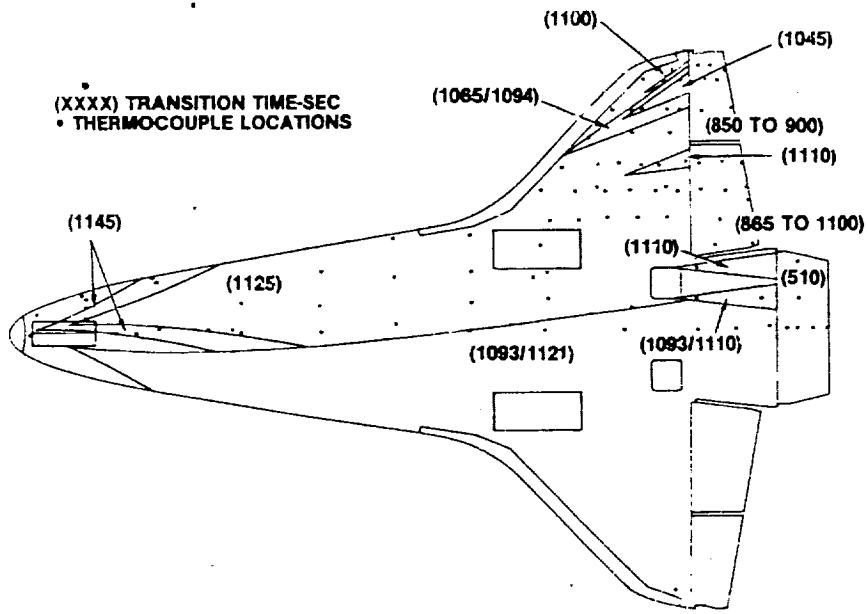


Figure 12.- STS-5 transition map.

ORIGINAL PAGE IS
OF POOR QUALITY

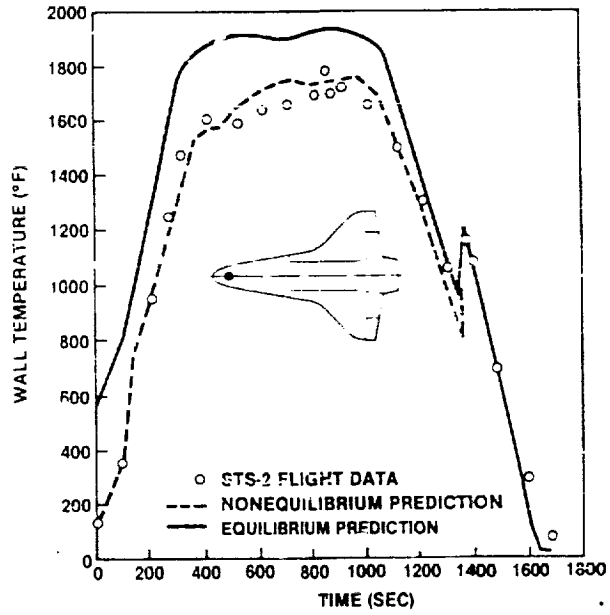


Figure 13.- STS-2 temperature history on fuselage lower-surface centerline at $X/L = 0.1$.

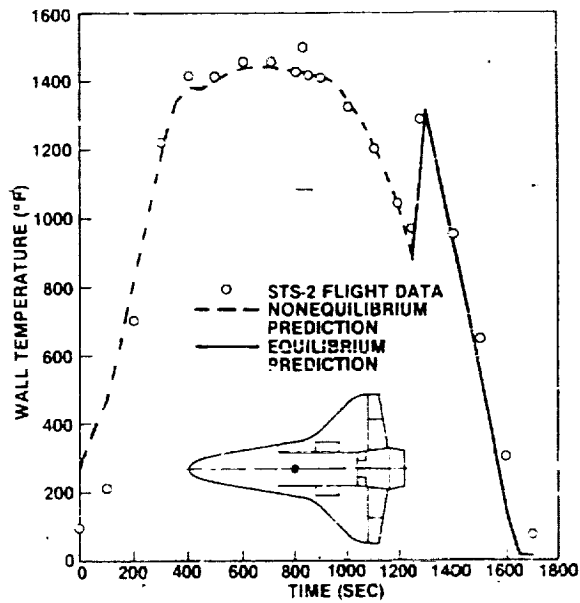


Figure 14.- STS-2 temperature history on fuselage lower-surface centerline at $X/L = 0.5$.

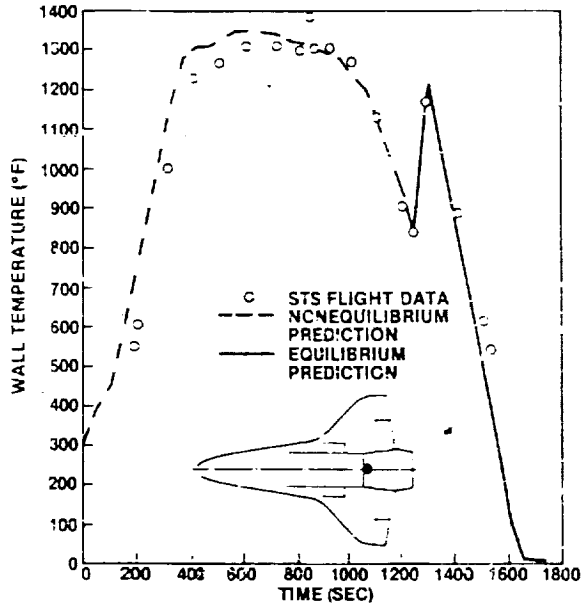


Figure 15.- STS-2 temperature history on fuselage lower-surface centerline at X/L = 0.9.

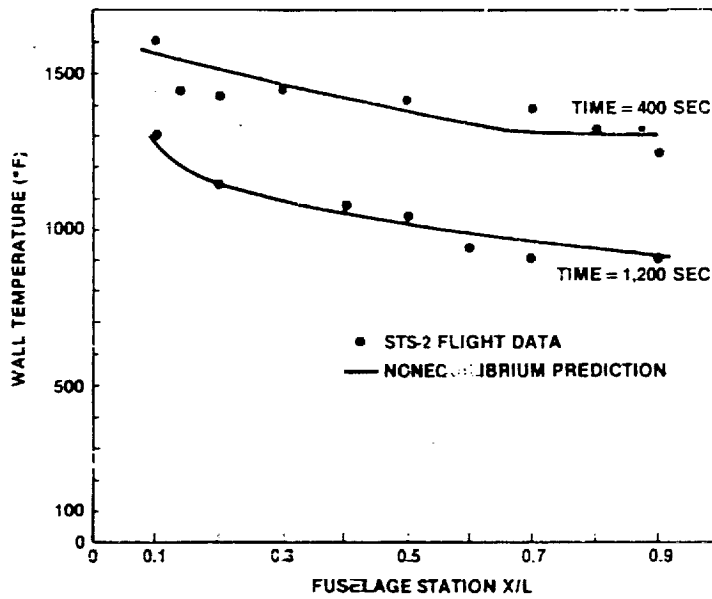


Figure 16.- Temperature distribution on fuselage lower-surface centerline 400 and 1,200 seconds after entry interface.

ORIGINAL PAGE IS
OF POOR QUALITY

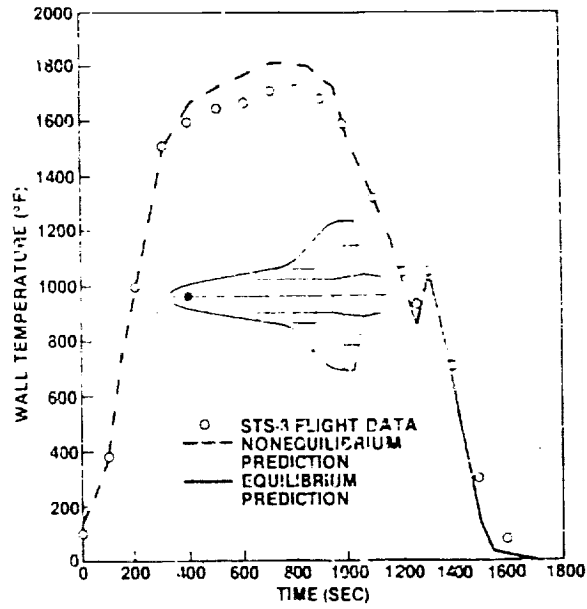


Figure 17.- STS-3 temperature history on fuselage lower-surface centerline at $X/L = 0.1$.

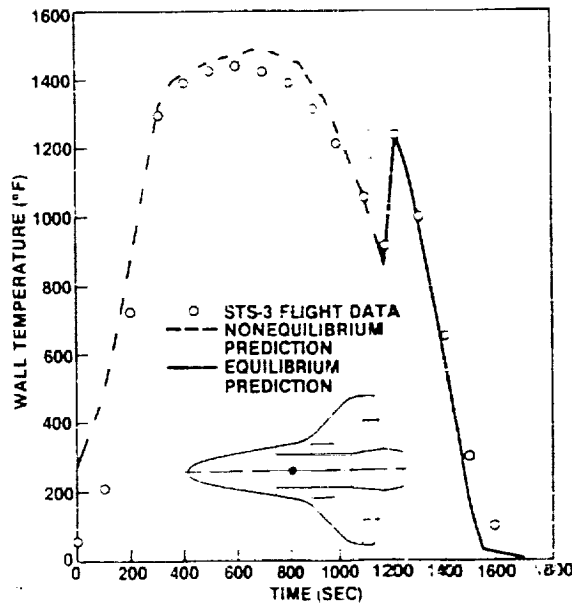


Figure 18.- STS-3 temperature history on fuselage lower-surface centerline at $X/L = 0.5$.

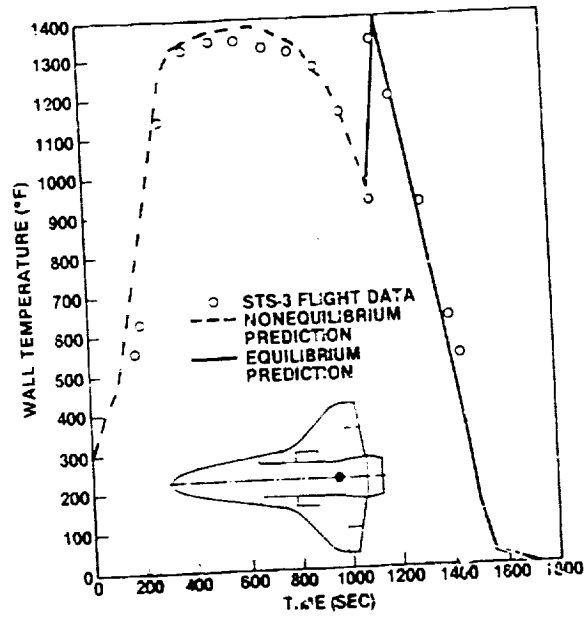


Figure 19.- STS-3 temperature history on fuselage lower-surface centerline at $X/L = 0.9$.

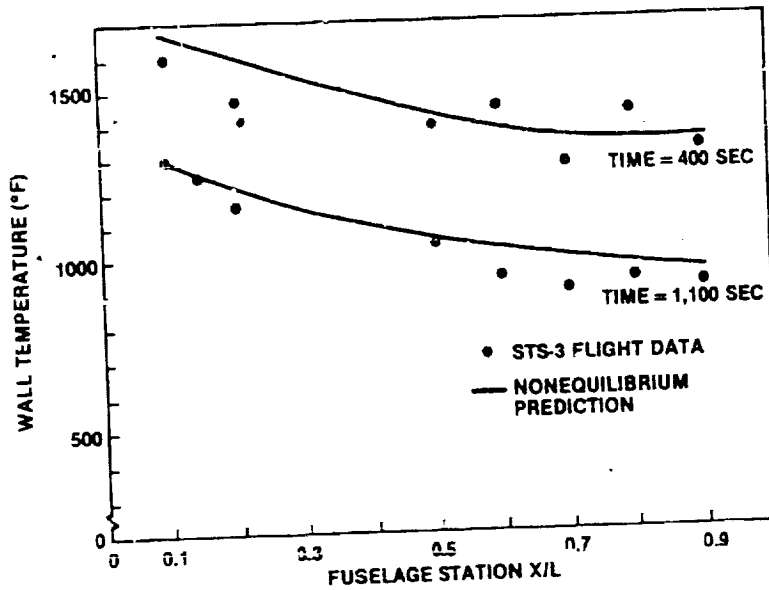


Figure 20.- Temperature distribution on fuselage lower-surface centerline 400 and 1,200 seconds after entry interface.

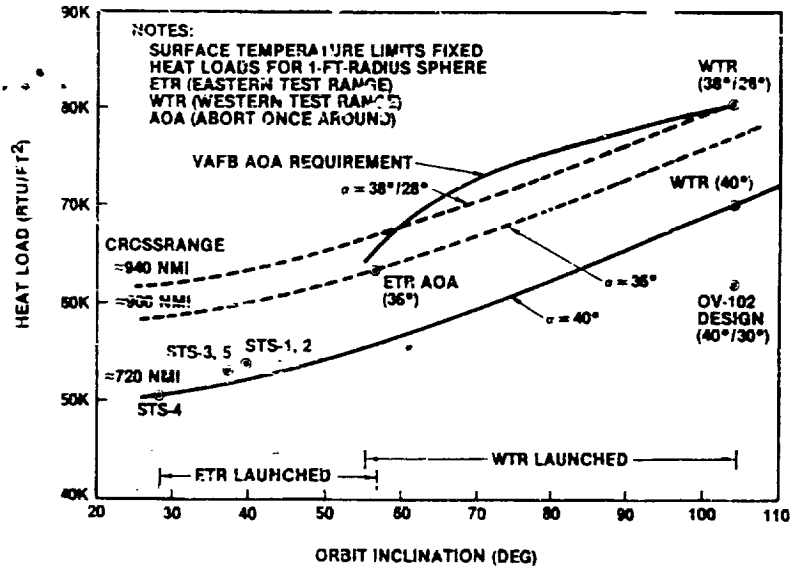


Figure 21.- Stagnation-point heat-load variation with orbit inclination and crossrange.